CrossMark

Dependence of the IRX-β Dust Attenuation Relation on Metallicity and Environment[*]

Irene Shivaei[1,4] , Behnam Darvish[2] , Zahra Sattari[3], Nima Chartab[3] , Bahram Mobasher[3], Nick Scoville[2] , and George Rieke[1]

[1] Steward Observatory, University of Arizona, Tucson, AZ 85721, USA; ishivaei@arizona.edu
[2] Cahill Center for Astrophysics, California Institute of Technology, Pasadena, CA 91125, USA
[3] Department of Physics and Astronomy, University of California at Riverside, Riverside, CA 92521, USA

Abstract

We use a sample of star-forming field and protocluster galaxies at $z = 2.0$–2.5 with Keck/MOSFIRE K-band spectra, a wealth of rest-frame ultraviolet (UV) photometry, and Spitzer/MIPS and Herschel/PACS observations, to dissect the relation between the ratio of infrared (IR) to UV luminosity (IRX) versus UV slope (β) as a function of gas-phase metallicity ($12 + \log(O/H) \sim 8.2$–8.7). We find no significant dependence of the IRX-β trend on environment. However, we find that at a given β, IRX is highly correlated with metallicity, and less correlated with mass, age, and specific star formation rate (sSFR). We conclude that, of the physical properties tested here, metallicity is the primary physical cause of the IRX-β scatter, and the IRX correlation with mass is presumably due to the mass dependence on metallicity. Our results indicate that the UV attenuation curve steepens with decreasing metallicity, and spans the full range of slope possibilities from a shallow Calzetti-type curve for galaxies with the highest metallicity in our sample ($12 + \log(O/H) \sim 8.6$) to a steep Small Magellanic Cloud (SMC)-like curve for those with $12 + \log(O/H) \sim 8.3$. Using a Calzetti (SMC) curve for the low (high) metallicity galaxies can lead to up to a factor of 3 overestimation (underestimation) of the UV attenuation and obscured star formation rate. We speculate that this change is due to different properties of dust grains present in the interstellar medium of low- and high-metallicity galaxies.

Unified Astronomy Thesaurus concepts: Interstellar dust extinction (837); Interstellar dust (836); Dust continuum emission (412); Galaxy evolution (594); Chemical abundances (224); Galaxy chemical evolution (580); Scaling relations (2031); Galaxy properties (615); Galaxy abundances (574); Star formation (1569)

1. Introduction

Dust attenuation and emission significantly modify our views of galaxies across cosmic time. The ratio of dust emission in infrared (L(IR)) to the observed ultraviolet (UV) emission (L(UV)), known as the infrared excess (IRX), is a measure of the UV dust attenuation. Additionally, the intrinsic UV continuum slope at $\lambda \sim 1600$–$2600\,\text{Å}$, β, is another measure of UV dust reddening, as the intrinsic slope is almost constant with age for massive stellar populations where the birth and death rates are in equilibrium (Leitherer et al. 1999). Therefore, by calibrating β using IRX, β becomes a powerful empirical diagnostic for recovering the total (attenuation-corrected) UV luminosity, using rest-frame UV observations alone (Meurer et al. 1999, hereafter MHC99). Such calibrations are central for high-redshift studies, where only optical/near-infrared (near-IR; i.e., rest-UV) observations have sufficient sensitivity to reach large samples of L_* and sub-L_* galaxies.

The effectiveness of an IRX-β relation depends on its validity for different types of galaxies across cosmic time. While the original MHC99 IRX-β relation applies to majority of galaxies, large scatters around this relation have been observed. Theoretical studies have shown that the IRX-β scatter may depend on the type of dust, gas metallicity, star formation history (SFH), dust-star geometry, and stellar population age (Popping et al. 2017; Safarzadeh et al. 2017; Narayanan et al. 2018;

Schulz et al. 2020). Observations have shown that the IRX-β relation varies with stellar mass (Bouwens et al. 2016, 2020; Reddy et al. 2018; Fudamoto et al. 2020), infrared (IR) luminosity (Buat et al. 2012; Casey et al. 2014), age (Siana et al. 2009; Reddy et al. 2010; Shivaei et al. 2015), redshift (Capak et al. 2015; Pannella et al. 2015), and intrinsic β_0 (β for a dust-free system; Boquien et al. 2012; Reddy et al. 2018; Schulz et al. 2020). These variations are linked to the diversity of galaxies' attenuation curves, seen in previous studies (e.g., Kriek & Conroy 2013; Scoville et al. 2015; Battisti et al. 2020). The attenuation curve variations stem from two main sources: (a) different geometrical distributions of dust with respect to stars (and different dust optical depths), and (b) different dust grain properties, which affect the shape of the underlying extinction curve irrespective of the dust-star geometry (see the review by Salim & Narayanan 2020). While scenario (a) is extensively studied by comparing the attenuation curves of galaxies with different dust optical depths (references above), scenario (b) is less explored. Dust compositions are related to gas-phase element depletions and abundances (Jenkins 2009). Following this relation, Shivaei et al. (2020, hereafter S20) studied scenario (b) by deriving the attenuation curve of $z \sim 2$ galaxies in two different metallicity ($12 + \log(O/H)$) bins, while the dust optical depth distributions were kept the same. They found a steep SMC-like curve for galaxies with $12 + \log(O/H) \lesssim 8.5$, and a shallower Calzetti et al. (2000, hereafter C00)-like curve at $12 + \log(O/H) \gtrsim 8.5$.

The S20 results were based on rest-frame UV and optical data. In this work, we use Spitzer/MIPS and Herschel/PACS IR data as direct tracers of dust emission for a unique sample of field and protocluster galaxies with Keck/MOSFIRE observations. Our

[4] NASA Hubble fellow.

goal is to study the dependence of the IRX-β relation at $z \sim 2$ on metallicity, mass, age, and environment.

2. Sample and Data

Our sample is part of the spectroscopic survey of protocluster and field galaxies in the COSMOS and UDS fields presented in Darvish et al. (2020). The primary sample is selected from the narrow-band Hα emitting catalog of High-z Emission Line Survey (HiZELS; Sobral et al. 2014) with follow-up spectroscopy in K-band using Keck/MOSFIRE (PI: N. Scoville). Filler targets are selected to be star-forming galaxies (using color–color selections, e.g., near-UV (NUV)-r-J; Ilbert et al. 2013) with photometric redshifts at $z_{phot} \sim 1.7$–2.8. The parent sample consists of 30 protocluster members at $z \sim 2.2$ and 217 field galaxies. For survey details and protocluster identification refer to Darvish et al. (2020) and Z. Sattari et al. (2020, in preparation). We use the spectra and photometry to extract key parameters, as explained below, with uncertainties estimated as the standard deviation of 1000 Monte-Carlo realizations, unless otherwise stated.

Line measurements and metallicities—The 1D spectra are fitted with a triple Gaussian function for the Hα and the [N II]λ 6550, 6585 lines (Z. Sattari et al. 2020, in preparation). Oxygen abundances (12 + log(O/H)), or metallicities, are calculated from the ratio of [N II]λ 6585 to Hα, assuming the empirical calibrations of Pettini & Pagel (2004). The ratio is a good metallicity tracer in the local universe (e.g., Marino et al. 2013). However, as the calibrations are uncertain at high redshifts (e.g., Bian et al. 2018), the absolute metallicity values reported here should be taken with caution. We emphasize that using the [N II]-to-Hα ratio is robust when dividing galaxies into broad metallicity categories discussed in this Letter.

Photometry and spectral energy distribution (SED) parameters—Catalogs of COSMOS2015 (Laigle et al. 2016) and SPLASH-SXDF (v1.5; Mehta et al. 2018) are used for sources in COSMOS and UDS, respectively, to calculate UV properties (see below), and infer SED parameters. For the SED fitting, both catalogs use the Bruzual & Charlot (2003) templates, assuming a Chabrier initial mass function (IMF), a range of stellar metallicities, exponentially declining SFHs (the COSMOS15 catalog also assume delayed SFHs), and two attenuation curves, the C00 curve and a steeper curve (similar to the SMC curve). For details, we refer to the survey papers.

UV luminosity and β—To derive the UV continuum slope, β, and UV luminosity density (L_ν) at 1600 Å, we fit a power law to the photometry at rest-frame $\lambda = 1260$–2600 Å, $f_\lambda \propto \lambda^\beta$ (COSMOS and UDS have good rest-UV coverage with at least four photometric points in this range). We avoid the wavelength range of $\lambda = 1950$–2400 Å, as it may potentially be affected by the 2175 Å UV bump, seen in the attenuation curve of high-metallicity galaxies at these redshifts (Scoville et al. 2015; Battisti et al. 2020; Shivaei et al. 2020). Hereafter, νL_ν at 1600 Å is referred to as UV luminosity, L(UV).

IR luminosity—We use the public Spitzer/MIPS 24 μm images of the COSMOS Spitzer survey (S-COSMOS; Sanders et al. 2007)[5] and the Spitzer UKIDSS Ultra Deep Survey (SpUDS; PI: J. Dunlop).[6] For Herschel/PACS data, we use the

public images of the PACS Evolutionary Probe survey (PEP; Lutz et al. 2011)[7] in COSMOS and those of the fourth Hershel-SPIRE/SAG-1/Herschel Multi-tiered Extragalactic Survey (HerMES; Oliver et al. 2012)[8] in UDS. The pixel scale of MIPS 24 μm images is $1\rlap{.}{''}2 \times 1\rlap{.}{''}2$. We matched the pixel scales of PEP PACS images to those of HerMES PACS images, by smoothing them to $2\rlap{.}{''}4 \times 2\rlap{.}{''}4$ and $3'' \times 3''$ for the 100 μm and 160 μm images, respectively.

Due to the confusion and sensitivity limits of MIPS and PACS data, stacking is required to detect the IR emission of typical galaxies at $z \gtrsim 1$. Therefore, we stack the target images and perform aperture photometry, as described in Appendix A. To estimate the total IR luminosity, we fit the photometry with two sets of IR templates: (i) the locally calibrated IR templates of Rieke et al. (2009, hereafter R09) and, (ii) a library of the local low-metallicity galaxy templates from Lyu et al. (2016). The R09 luminous infrared galaxies (LIRGs) templates accurately fit our galaxies with high metallicities (12 + log(O/H) $\gtrsim$ 8.5), in agreement with other studies that support the use of local LIRG templates for massive, IR-bright galaxies at high redshifts (e.g., De Rossi et al. 2018). However, in Appendix B we show that the lower metallicity galaxies fit better with the low-metallicity local templates. Ultimately, the best-fit template is determined through a minimum χ^2 method and the total IR luminosity is calculated by integrating the best-fit template at $\lambda = 8$–1000 μm.

Final sample—The final sample consists of objects with $>3\sigma$ detection in Hα and [N II], required for robust metallicity calculations. We remove targets that are classified as mergers by visual inspection of the spectra and/or images, IR active galactic nucleus (AGN; using the Donley et al. 2012 criteria), X-ray AGN (from the COSMOS and UDS catalogs), and optical AGN ([N II]/Hα > 0.5). Furthermore, as ultraluminous infrared galaxies (ULIRGs) are known to be outliers in the IRX-β relation (e.g., Casey et al. 2014), we remove targets with $>3\sigma$ detection in Herschel/PACS 100 μm or 160 μm (corresponding to galaxies with L(IR) $\gtrsim 10^{12} L_\odot$). The final sample consists of 62 field and 13 protocluster galaxies at $z = 2.0$–2.5.

3. IRX-β as a Function of Environment and Galaxy Properties

Average IRX values are derived in two metallicity bins divided at 12 + log(O/H) = 8.5, and four β bins at $\langle \beta \rangle \sim -1.4, -0.9, -0.5, 0.2$. We choose the metallicity limit of 12 + log(O/H) = 8.5 as it has been shown that $z \sim 2$ galaxies with metallicities below and above this limit have different attenuation curves (Shivaei et al. 2020). The exact β boundaries are chosen randomly from the ranges shown in the left panel of Figure 1 for 100 trials. The details of sampling are described in Appendix C. We later exclude the reddest β bin that includes galaxies with $\beta \gtrsim 0$ from the analysis, as their βs are uncertain and likely affected significantly by the older stellar populations, owing to their lower specific star formation rate (sSFR; average of 0.09 Gyr^{-1}) and older ages (average of 1 Gyr) compared to the rest of the sample.

The right panel of Figure 1 shows the IRX-β in the two bins of metallicity for the full sample (field and protocluster galaxies), and for the field galaxies only. We do not find any significant difference between the IRX-β values of the full
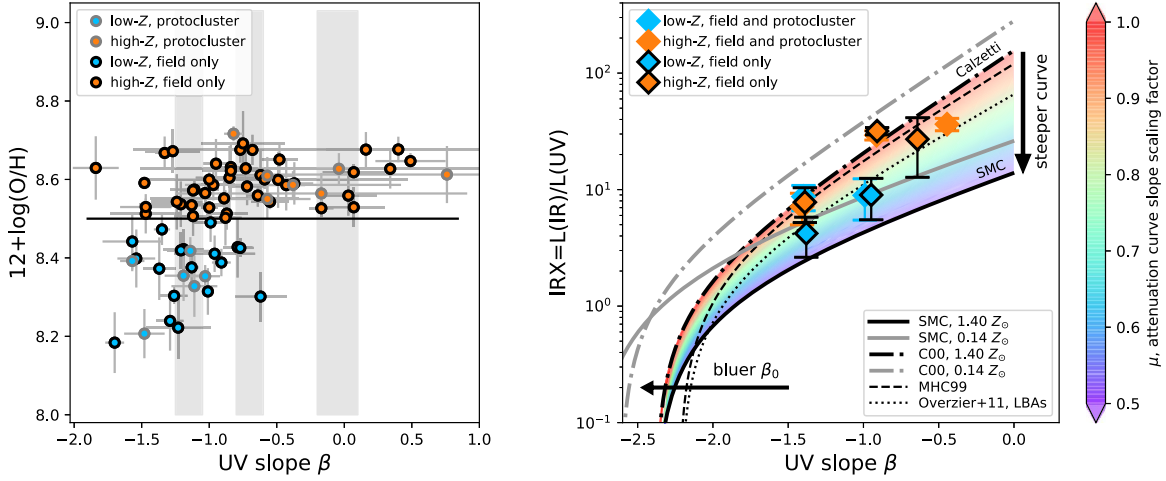
Figure 1. Left panel: metallicity vs. β for the field and protocluster galaxies. The metallicity and β boundaries used to divide the sample into the bins displayed in the right panel are shown with a black line and gray regions, respectively. β boundaries are chosen randomly within the gray regions for 100 trials (see Appendix C). Right panel: IRX-β for the full sample at $z = 2.0$–2.5 (no edge-color symbols) and only field galaxies (black-edged symbols) at $12 + \log(O/H) < 8.5$ (low-Z, blue) and $12 + \log(O/H) > 8.5$ (high-Z, orange). Galaxies with $\beta \gtrsim 0$ are not shown in the plot. The original MHC99 curve (Meurer et al. 1999) is shifted by 0.24 dex upward (Reddy et al. 2018) to convert the far-IR luminosity in that study to the total IR luminosity assumed here. The SMC (Gordon et al. 2003) and Calzetti et al. (2000, C00) relations are taken from Reddy et al. (2018), assuming a constant star formation history and an age of 100 Myr for stellar populations with two different stellar metallicities (0.14 and 1.40 $Z_\odot$). A lower stellar metallicity results in a bluer intrinsic β_0 and hence, shifts the IRX-β curves to the left. At a fixed β_0, corresponding to that of the 1.40 $Z_\odot$ model, we show the loci of attenuation curves with different slopes in between the C00 and SMC slopes, with rainbow colors. The colors show the power-law slope deviation factor, μ, where $\mu = 1$ corresponds to the C00 curve (black dashed–dotted line) and the steepest curve shown has a $\mu = 0.5$, resembling an SMC-like curve (black solid line). These curves are reproduced by scaling the exponent of the C00, 1.40 $Z_\odot$ relation as IRX $= 1.44 \times [10^{0.4(2.14\beta+5.10)\mu}]$. The Overzier et al. (2011) curve for Lyman break analogs (LBAs) is also shown for reference. Our low-metallicity stacks agree well with the SMC, 0.14 $Z_\odot$ curve, while the high-metallicity stacks lie closer to the C00, 1.40 $Z_\odot$ and the MHC99 curves.
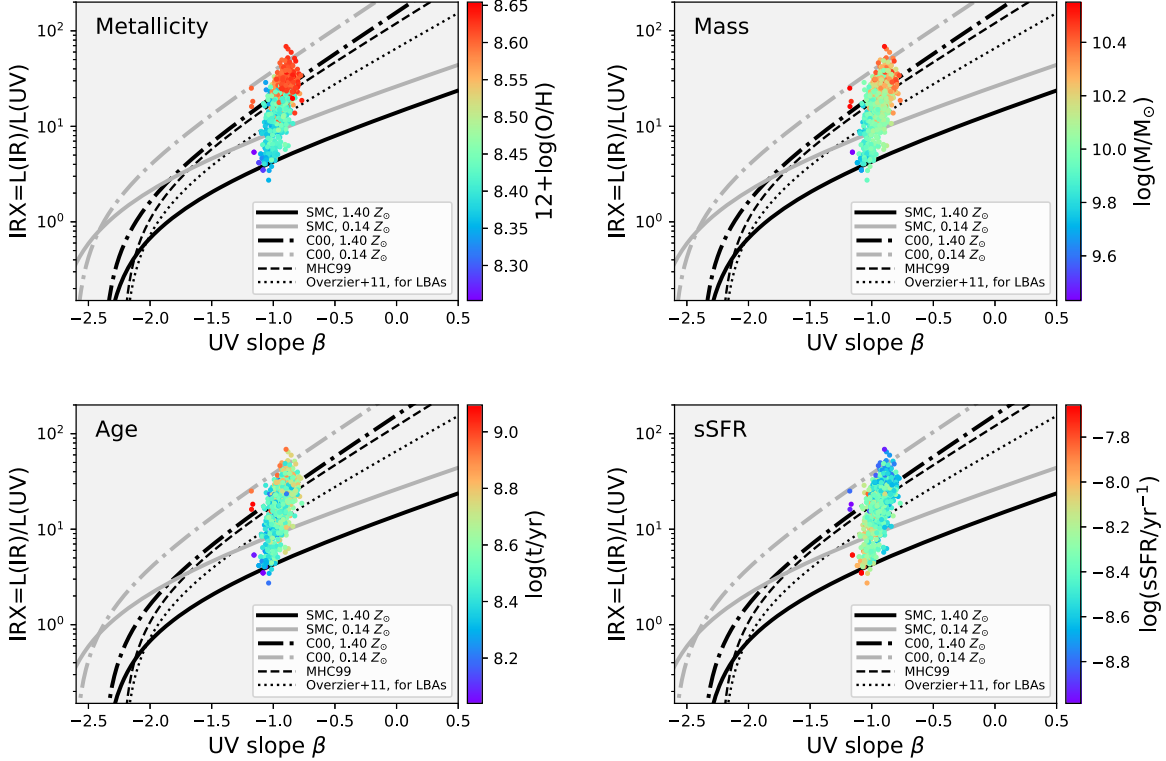

Figure 2. IRX-β at $\beta \sim [-1.2, -0.7]$ color-coded by metallicity, mass, age, and sSFR, as indicated. Points are measured for bootstrapped samples in different bins of metallicity, as explained in Appendix C. Curves are the same as in Figure 1.

sample and those of the field galaxies only, suggesting that the trend is independent of the environment. On the other hand, the low-metallicity galaxies in both samples agree better with the SMC relations, while the high-metallicity ones at the same β favor the C00 and MHC99 relations. Figure 1 shows the range

of IRX-β relations for different attenuation curves (with slopes in between the SMC and C00 slopes), and different intrinsic β_0 values.

The change in IRX with metallicity is less significant at $\beta \lesssim -1.2$, both because the IRX-β curves are less distinguishable in
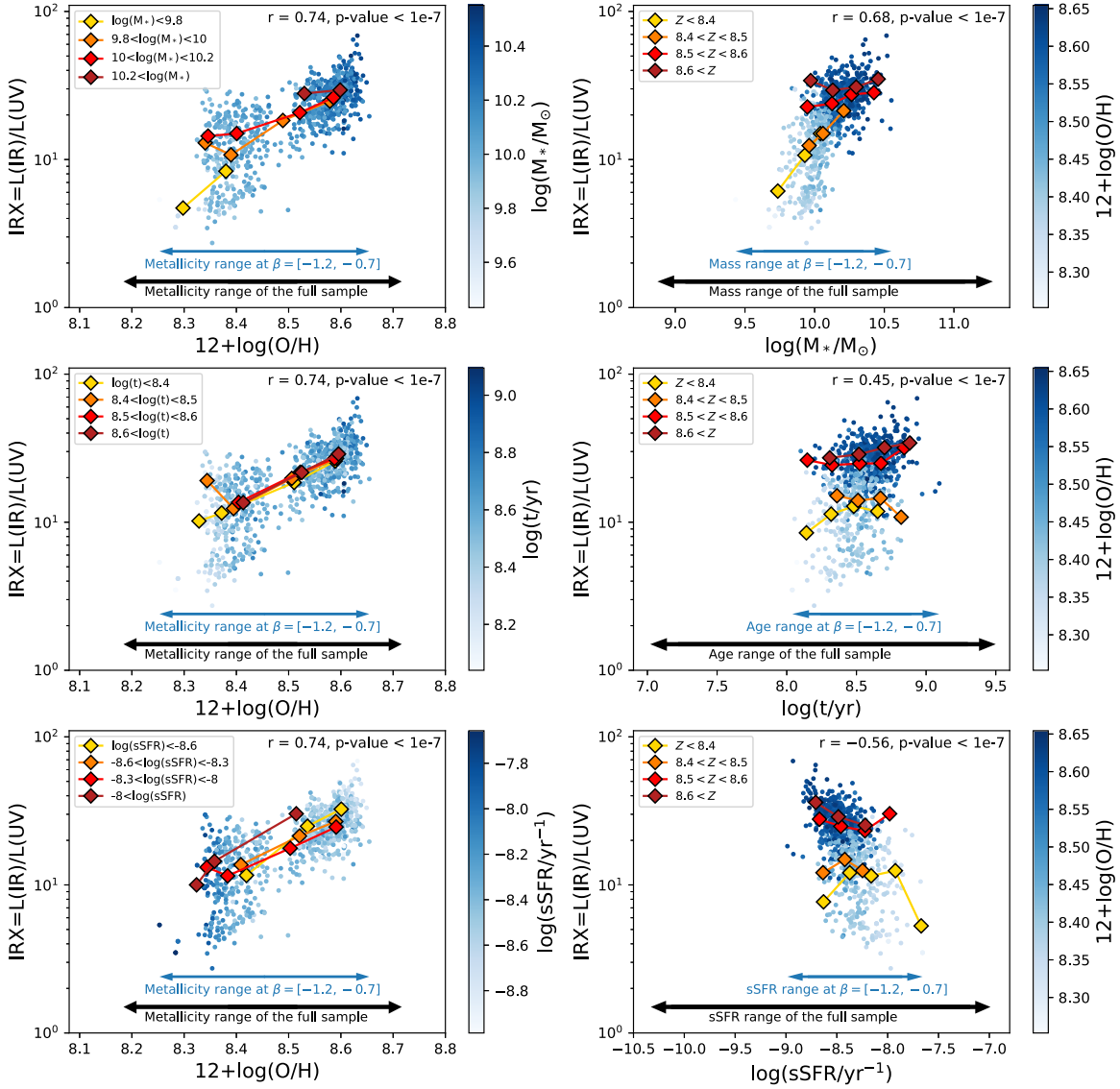
Figure 3. Left column: IRX vs. metallicity at $-1.2 < \beta < -0.7$ for the measurements in Figure 2 (blue circles). The average values in narrow bins of mass, age, and sSFR (top to bottom, respectively) are shown with diamonds. The Pearson correlation factors (r) and corresponding p-values for the blue points are also shown. The ranges of the parameters at $-1.2 < \beta < -0.7$ and those of the full sample are shown with blue and black arrows, respectively. Right column from top to bottom: IRX vs. mass, age, and sSFR with averages in narrow bins of metallicity. Symbols are the same as the left column.

this range, and also due to our sample incompleteness at these blue βs. The HiZELS parent sample at $z \sim 2$ is complete down to $M_* \sim 10^{9.7} M_\odot$ (Sobral et al. 2012, 2014), which corresponds to $\beta \sim -1.3$ (Fudamoto et al. 2020) and $12 + \log(\mathrm{O/H}) \sim 8.3$ (Sanders et al. 2018). As we specifically select emission-line detected galaxies, the average IRX at $\beta < -1.3$ and $12 + \log(\mathrm{O/H}) < 8.3$ is possibly biased toward higher values, suffering from a Malmquist bias.

We further investigate the IRX-β scatter as a function of other galaxy properties at $\beta \sim -1.2$ to -0.7, as at this β range our sample is complete and includes galaxies with a wide range of metallicities. We divide the sample into multiple metallicity bins, and bootstrap resample from each bin to stack the IR data and calculate IRX. We refer to Appendix C for the sampling details. Panels of Figure 2 show the IRX-β measurements color-coded with metallicity, mass, age, and sSFR. IRX increases significantly with increasing metallicity at a given β, such that as metallicity increases, galaxies occupy the full

range of attenuation curves from the SMC to the MHC99 and C00 relations. The same trend, but weaker, is seen with increasing stellar mass and age and decreasing sSFR.[9]

4. Which Parameter Drives the IRX-β Scatter?

It is expected, from a physical point of view, that dust attenuation properties correlate with gas abundances. To confirm this statement, we perform a partial correlation test to determine whether the IRX dependence on metallicity remains when the other parameters are held fixed. We divide the realizations in Figure 2 into a series of bins with narrow ranges in metallicity, mass, age, and sSFR. We calculate the mean IRX in bins of mass, age, and sSFR as a function of metallicity (diamonds in the left column of Figure 3), and in

---

[9] The SED-inferred SFRs and ages are highly sensitive to the assumed attenuation curve (Shivaei et al. 2018, 2020). However, our SFRs and ages are less affected, as a range of attenuation curves is assumed in the SED fittings used in this work (Section 2).

bins of metallicity as a function of the other three parameters (diamonds in the right column of Figure 3). The left column of Figure 3 shows that the IRX correlation with metallicity remains unchanged even if we look at it in narrow bins of mass, age, and sSFR. On the other hand, the right panels show that any correlations with mass, age, and sSFR are much weaker when observed in bins of metallicity. This indicates that among these four parameters, metallicity has the strongest correlation with IRX and UV attenuation.

The Pearson correlation factor and the range of parameters covered at the given β reinforce the conclusions we have already drawn. IRX has the largest correlation factor with metallicity (shown in the corners of plots in Figure 2), and the widest metallicity range, comparable to the metallicity range of the full sample. Variations in mass, sSFR, and age move galaxies more significantly along the IRX-β curves (i.e., changing both IRX and β), as opposed to changing IRX at a given β—which explains the small dynamic ranges of these properties at this β bin compared to the range of the properties in the full sample (blue and black arrows in Figure 3, respectively).

We conclude that a major factor in the scatter of the IRX-β relation is metallicity, as metallicity reflects the properties of small dust grains that determine the steepness of the attenuation curve in the UV (e.g., Gordon et al. 1997; Zelko & Finkbeiner 2020). At low metallicities, the intense UV radiation in the interstellar medium and the reduced gas and dust shielding from the UV radiation, due to lower molecular fraction (ratio of molecular to total gas mass), make the environment favorable to shatter large dust grains into small ones, resulting in a steep rise in the UV attenuation curve (Shivaei et al. 2020).

5. Implications for UV Dust Corrections at High Redshifts

The IRX-β relation is a powerful tool for correcting the observed UV luminosities for attenuation. Figure 4 shows the ratio of predicted $L(\mathrm{IR})$ from UV observations, to the observed $L(\mathrm{IR})$, integrated at $\lambda = 8–1000\,\mu\mathrm{m}$. The predicted $L(\mathrm{IR})$, $L(\mathrm{IR})_{A_{1600}}$, is calculated as

$$L(\mathrm{IR})_{A_{1600}} = \gamma \times L(\mathrm{UV}) \times (10^{0.4\,A_{1600}} - 1), \qquad (1)$$

where $L(\mathrm{UV})$ is the observed UV luminosity at 1600 Å, A_{1600} is the total attenuation at 1600 Å calculated using β and assuming an attenuation curve, and γ is the bolometric correction to convert the absorption at 1600 Å to total absorbed UV flux. We adopt $\gamma = 2.13$ from the IRX calibrations of Hao et al. (2011) with Balmer decrement-corrected Hα luminosities. We assume different $\beta - A_{1600}$ relations for galaxies below and above $12 + \log(\mathrm{O/H}) = 8.5$: two C00-like relations with solar-metallicity populations for the high-metallicity points (MHC99 and the S20 high-metallicity curve), and two relations that follow a steeper SMC-like curve and sub-solar stellar populations (the SMC relation of Reddy et al. 2018 and the S20 low-metallicity curve). The good agreement between the predicted and observed $L(\mathrm{IR})$ in Figure 4 indicates that, *on average*, galaxies with $12 + \log(\mathrm{O/H})$ below and above 8.5 (corresponding to $M_* \sim 10^{10.4}\,M_\odot$, owing to the mass–metallicity relation; e.g., Sanders et al. 2018) follow a steep SMC-like and a shallower C00-like curves, respectively. In reality, there is an infinite range of attenuation curve
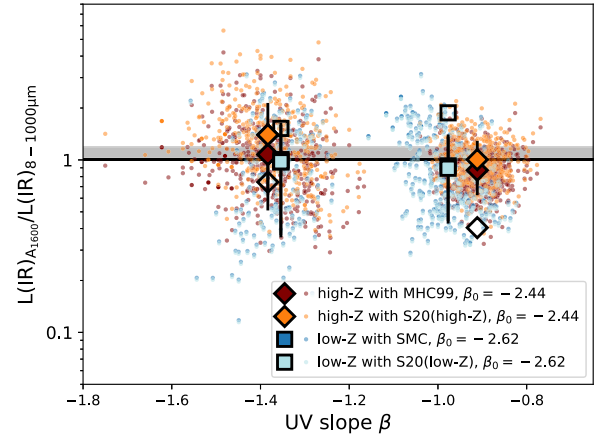

Figure 4. Ratio of predicted ($L(\mathrm{IR})_{A_{1600}}$, Equation (1)) to measured ($L(\mathrm{IR})_{8–1000\,\mu m}$) IR luminosities as a function of β. Each small circle is a random realization in metallicity and β bins, calculated in the same way as in Figure 2 with the difference of having a single metallicity division at $12 + \log(\mathrm{O/H}) = 8.5$ (Appendix C). Averages in each metallicity and β bin are shown with large symbols. Dark red and orange symbols show high-metallicity stacks, for which $L(\mathrm{IR})_{A_{1600}}$ is calculated using the MHC99 relation and the high-metallicity relation of Shivaei et al. (2020, S20), respectively. Dark blue and light blue symbols (which are indistinguishable) show low-metallicity stacks, for which $L(\mathrm{IR})_{A_{1600}}$ is calculated using the SMC relation from Reddy et al. (2018) and Gordon et al. (2003) and the S20 low-metallicity relation, respectively. The horizontal line is unity and the gray region reflects the range of different bolometric corrections ($\gamma \sim 1.79–2.07$, Equation (1)) from Reddy et al. (2018) and MHC99. The empty squares (diamonds) show the calculations using the MHC99 (SMC) relation for the low-(high-)metallicity galaxies, which result in overestimation (underestimation) of $L(\mathrm{IR})_{A_{1600}}$.

possibilities and, based on the results of this study, their slopes correlate with galaxies metallicities. We show in Figure 4 (empty symbols) that using a C00-like attenuation curve for the low-metallicity galaxies would overestimate the predicted $L(\mathrm{IR})_{A_{1600}}$ up to a factor of $\sim$3. These results are specifically important for high-redshift studies, as the galaxies at higher redshifts have lower metallicities at a given mass (Maiolino & Mannucci 2019), and presumably more SMC-like stellar dust attenuation properties.

Appendix A
MIPS and PACS Stacking and Aperture Photometry

Stacking—Due to the confusion and sensitivity limits of Spitzer/MIPS and Herschel, stacking is required to detect the IR emission of typical galaxies at $z \gtrsim 1$. To perform stacking, we construct 40×40 pixel subimages centered at our targets' optical coordinates. When necessary, the images are shifted by sub-pixel values to accurately center the targets. For MIPS images, we use a list of prior sources with signal-to-noise ratio (S/N) of >3 in Spitzer/IRAC 1 and 2. For PACS images, we use a list of priors with S/N of >3 in MIPS 24 μm. Using the prior lists, we model the emission of the companion sources (all of the prior objects, except for the target) by performing scaled point-spread function (PSF) photometry on the subimages. By subtracting the companion model images from the original
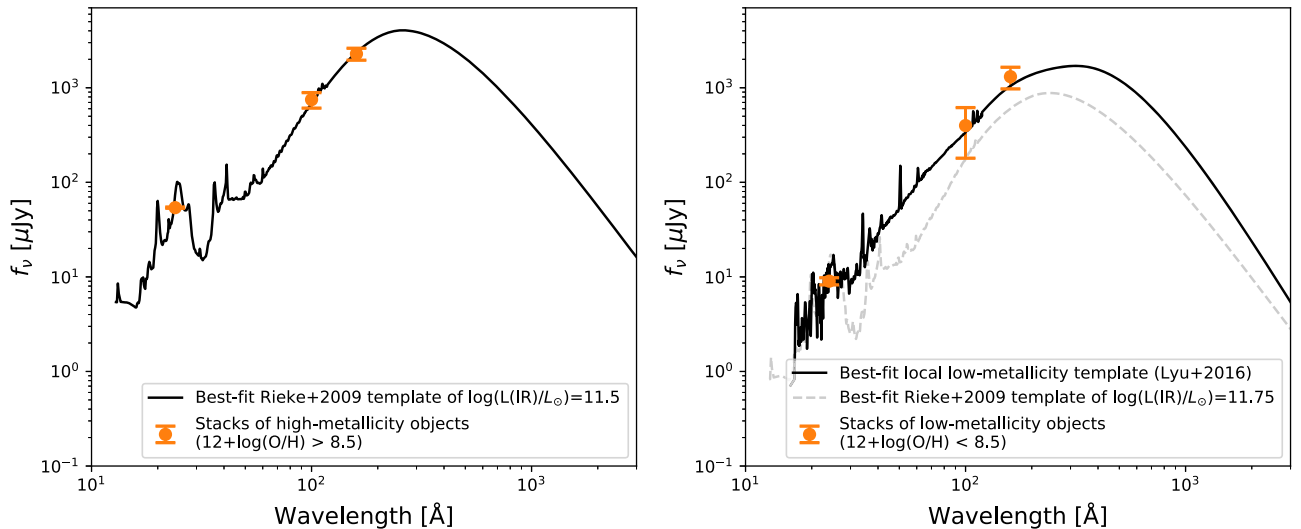
Figure 5. The best-fit IR SEDs IR to the 24, 100, and 160 μm stacked photometry (orange circles) of our galaxies with metallicities above (left panel) and below (right right) of $12 + \log(O/H) = 8.5$. The LIRG templates of Rieke et al. (2009) accurately reproduce the observed photometry of our high-metallicity galaxies (left panel), while their 7.7 μm polycyclic aromatic hydrocarbon (PAH) intensity is overestimated for the low-metallicity galaxies (gray curve in the right plot). We use a library of local low-metallicity templates from Lyu et al. (2016) to fit our low-metallicity galaxies (black curve in the right plot).

image, we make clean subimages that only include our target. Using the clean subimages, we perform 3σ-trimmed (clipped) mean stacking. Trimmed mean is used to ensure the mean is not biased toward outliers.

Aperture photometry—To measure fluxes and their associated errors, we perform aperture photometry on the stacked images. We use an aperture size of $3''$, $7.2''$, and $9''$ for the 24 μm, 100 μm, and 160 μm images, respectively. The best aperture sizes are determined by performing aperture photometry with different aperture sized on the stacked images of all the sources in each band and choosing the aperture with the highest S/N in each band. For the 24 μm stacks, we measure the aperture correction (the amount of light that is lost outside of the aperture) from the growth curve of the 24 μm stacked image of all the source. For the PACS aperture corrections, we use the calculated PACS encircled energy fractions (EEFs) of Balog et al. (2014, their Table 2). The flux errors are estimated as the standard deviation of the fluxes measured in 100 apertures with the same radii as the source aperture radius, located at random positions away from the center of the image (where the source is) by more than 1 FWHM of the image PSF.

Appendix B
IR Templates

We use the locally calibrated IR templates of Rieke et al. (2009, R09) and a library of the local low-metallicity galaxies template from Lyu et al. (2016) to fit our high- and low-metallicity galaxies, respectively. The R09 templates are limited to those with luminosities of $10^{10.5}$–$10^{12} L_\odot$, as previous studies have shown that these templates accurately match the IR emission of LIRGs at high redshifts (e.g., De Rossi et al. 2018).[10] The left panel of Figure 5 show the fit to the stacked photometry of our sample with $12 + \log(O/H) > 8.5$.

On the other hand, the local LIRG and ULIRG templates are not appropriate for low-metallicity and low-mass galaxies at

high redshifts. Shivaei et al. (2017) showed that the intensity of the 7.7 μm aromatic band emission, which is traced by MIPS 24 μm at $z \sim 2$, is significantly suppressed at metallicities of $12 + \log(O/H) \lesssim 8.5$[11] compared to that in the higher metallicity galaxies at the same redshift and to that in the locally calibrated templates of LIRGs and ULIRGs. The right panel of Figure 5 shows that the R09 templates can not reproduce the observed 24, 100, and 160 μm photometry of sources with $12 + \log(O/H) < 8.5$. Therefore, for our low-metallicity galaxies, we use a library of 19 templates of local low-metallicity galaxies from Lyu et al. (2016). These galaxies were selected from the Dwarf Galaxy Survey (DGS; Madden et al. 2013) to have high enough signal-to-noise Spitzer/IRS spectra. The IR templates are constructed by combining Herschel and WISE photometry with Spitzer/IRS spectra. The right panel of Figure 5 shows how well these templates fit our observed low-metallicity photometry. If the 24 μm data is excluded from the fits, the inferred IR luminosities from the best-fit local low-metallicity templates and those from the best-fit R09 templates are consistent with each other within the uncertainties.

Appendix C
Sampling Methodology

To avoid introducing biases in the results by arbitrarily choosing fixed β and metallicity boundaries, we resample the data in many trials using different metallicity and β boundaries, as follows. In Figure 1, the sample is divided into two metallicity bins at $12 + \log(O/H) = 8.5$ and into four β bins (however, the reddest β bin is later excluded from the analysis). We perform 100 trials to randomly select boundaries of β from the following intervals: $\beta = [-1.25, -1.05]$, $[-0.8, -0.6]$, and $[-0.2, 0.1]$ (Figure 1, left panel). The width of the β ranges are chosen to reflect the typical uncertainty of β in each range. Then for each realization, we stack the IR images, choose the IR template with the least χ^2 value from the best-fit R09

---

[10] IR luminosities estimated from other commonly used templates, such as the Chary & Elbaz (2001) and Elbaz et al. (2011) templates, are consistent with those derived from the R09 templates (see Reddy et al. 2012 for templates comparison).

[11] The metallicity here is estimated using the ratio of [N II]/Hα and the calibrations of Pettini & Pagel (2004).

template and the best-fit low-metallicity template, and calculate the IR luminosity. If all three of the MIPS and PACS stacks are undetected for a subsample, that realization is removed from the analysis due to unconstrained IR luminosity. The IRX value for each realization is the ratio of the IR luminosity to 3σ-trimmed average UV luminosity. Finally, the average and standard deviation of the IRX distribution are taken as the IRX and its error, respectively, and the average β and metallicity are calculated in the right panel of Figure 1.

The same sampling procedure is used for the data points in Figures 2 and 3, with two differences: (1) to avoid biases due to arbitrarily chosen metallicity bins, we use five different metallicity boundaries at $12 + \log(O/H) = 8.35$–8.55 with 0.05 dex intervals, and (2) we bootstrap resample from each bin to stack the IR data and calculate IRX. The exact minimum and maximum βs in each metallicity bin are randomly chosen from the ranges of $\beta = [-1.25, -1.05]$ and $[-0.8, -0.6]$, respectively, for each bootstrapped sample (repeated 100 times). Then, IRX and average β, metallicity, mass, age, and sSFR (sSFR = SFR/M_*) are calculated for each realization, and shown as circles in Figures 2 and 3. Figure 4 shows the same bootstrapped realizations but divided at a single metallicity boundary and into two β bins.

ORCID iDs

Irene Shivaei ⓘ https://orcid.org/0000-0003-4702-7561
Behnam Darvish ⓘ https://orcid.org/0000-0003-4919-9017
Nima Chartab ⓘ https://orcid.org/0000-0003-3691-937X
Nick Scoville ⓘ https://orcid.org/0000-0002-0438-3323
George Rieke ⓘ https://orcid.org/0000-0003-2303-6519

References

Balog, Z., Müller, T., Nielbock, M., et al. 2014, ExA, 37, 129
Battisti, A. J., Cunha, E. d., Shivaei, I., & Calzetti, D. 2020, ApJ, 888, 108
Bian, F., Kewley, L. J., & Dopita, M. A. 2018, ApJ, 859, 175
Boquien, M., Buat, V., Boselli, A., et al. 2012, A&A, 539, A145
Bouwens, R., Gonzalez-Lopez, J., Aravena, M., et al. 2020, ApJ, 902, 112
Bouwens, R. J., Aravena, M., Decarli, R., et al. 2016, ApJ, 833, 72
Bruzual, G., & Charlot, S. 2003, MNRAS, 344, 1000
Buat, V., Noll, S., Burgarella, D., et al. 2012, A&A, 545, A141
Calzetti, D., Armus, L., Bohlin, R. C., et al. 2000, ApJ, 533, 682
Capak, P. L., Carilli, C., Jones, G., et al. 2015, Natur, 522, 455
Casey, C. M., Scoville, N. Z., Sanders, D. B., et al. 2014, ApJ, 796, 95
Chary, R., & Elbaz, D. 2001, ApJ, 556, 562
Darvish, B., Scoville, N. Z., Martin, C., et al. 2020, ApJ, 892, 8
De Rossi, M. E., Rieke, G. H., Shivaei, I., Bromm, V., & Lyu, J. 2018, ApJ, 869, 4
Donley, J. L., Koekemoer, A. M., Brusa, M., et al. 2012, ApJ, 748, 142
Elbaz, D., Dickinson, M., Hwang, H. S., et al. 2011, A&A, 533, A119
Fudamoto, Y., Oesch, P. A., Magnelli, B., et al. 2020, MNRAS, 491, 4724
Gordon, K. D., Calzetti, D., & Witt, A. N. 1997, ApJ, 487, 625
Gordon, K. D., Clayton, G. C., Misselt, K. A., Landolt, A. U., & Wolff, M. J. 2003, ApJ, 594, 279
Hao, C.-N., Kennicutt, R. C., Johnson, B. D., et al. 2011, ApJ, 741, 124
Ilbert, O., McCracken, H. J., Le Fèvre, O., et al. 2013, A&A, 556, A55
Jenkins, E. B. 2009, ApJ, 700, 1299
Kriek, M., & Conroy, C. 2013, ApJL, 775, L16
Laigle, C., McCracken, H. J., Ilbert, O., et al. 2016, ApJS, 224, 24
Leitherer, C., Schaerer, D., Goldader, J. D., et al. 1999, ApJS, 123, 3
Lutz, D., Poglitsch, A., Altieri, B., et al. 2011, A&A, 532, A90
Lyu, J., Rieke, G. H., & Alberts, S. 2016, ApJ, 816, 85
Madden, S. C., Rémy-Ruyer, A., Galametz, M., et al. 2013, PASP, 125, 600
Maiolino, R., & Mannucci, F. 2019, A&A Rev, 27, 3
Marino, R. A., Rosales-Ortega, F. F., Sánchez, S. F., et al. 2013, A&A, 559, A114
Mehta, V., Scarlata, C., Capak, P., et al. 2018, ApJS, 235, 36
Meurer, G. R., Heckman, T. M., & Calzetti, D. 1999, ApJ, 521, 64
Narayanan, D., Davé, R., Johnson, B. D., et al. 2018, MNRAS, 474, 1718
Oliver, S. J., Bock, J., Altieri, B., et al. 2012, MNRAS, 424, 1614
Overzier, R. A., Heckman, T. M., Wang, J., et al. 2011, ApJL, 726, L7
Pannella, M., Elbaz, D., Daddi, E., et al. 2015, ApJ, 807, 141
Pettini, M., & Pagel, B. E. J. 2004, MNRAS, 348, L59
Popping, G., Puglisi, A., & Norman, C. A. 2017, MNRAS, 472, 2315
Reddy, N., Dickinson, M., Elbaz, D., et al. 2012, ApJ, 744, 154
Reddy, N. A., Erb, D. K., Pettini, M., Steidel, C. C., & Shapley, A. E. 2010, ApJ, 712, 1070
Reddy, N. A., Oesch, P. A., Bouwens, R. J., et al. 2018, ApJ, 853, 56
Rieke, G. H., Alonso-Herrero, A., Weiner, B. J., et al. 2009, ApJ, 692, 556
Safarzadeh, M., Hayward, C. C., & Ferguson, H. C. 2017, ApJ, 840, 15
Salim, S., & Narayanan, D. 2020, arXiv:2001.03181
Sanders, D. B., Salvato, M., Aussel, H., et al. 2007, ApJS, 172, 86
Sanders, R. L., Shapley, A. E., Kriek, M., et al. 2018, ApJ, 858, 99
Schulz, S., Popping, G., Pillepich, A., et al. 2020, MNRAS, arXiv:2001.04992
Scoville, N., Faisst, A., Capak, P., et al. 2015, ApJ, 800, 108
Shivaei, I., Reddy, N., Rieke, G., et al. 2020, ApJ, 899, 117
Shivaei, I., Reddy, N. A., Shapley, A. E., et al. 2017, ApJ, 837, 157
Shivaei, I., Reddy, N. A., Siana, B., et al. 2018, ApJ, 855, 42
Shivaei, I., Reddy, N. A., Steidel, C. C., & Shapley, A. E. 2015, ApJ, 804, 149
Siana, B., Smail, I., Swinbank, A. M., et al. 2009, ApJ, 698, 1273
Sobral, D., Best, P. N., Smail, I., et al. 2014, MNRAS, 437, 3516
Sobral, D., Smail, I., Best, P. N., et al. 2012, MNRAS, 428, 1128
Zelko, I. A., & Finkbeiner, D. P. 2020, arXiv:2009.11869